

(NASA-CR-195952) SEMI-SPAN MODEL
TESTING IN THE NATIONAL TRANSONIC
FACILITY Semiannual Status Report
(North Carolina State Univ.) 21 p

N94-34300

Unclass

G3/34 0010375

Semi-annual Status Report-May 1994
Cooperative Agreement No. NCC1 - 169

Name and address of Institution:

North Carolina State University
Mechanical & Aerospace Engineering Department
Raleigh NC 27695-7910
(919) 515 - 5667

100-100000-100000
100-100000-100000
21P

Title: Semi-Span Model Testing in the National Transonic Facility

Principal Investigator:

Dr. Ndaona Chokani

Research Assistant:

William E. Milholen II

NASA Technical Officer:

Jassim A. Al-Saadi

NASA Langley Research Center
High Reynolds Number Aerodynamics Branch
AAD MS 267
(804) 864 - 5164

Introduction

Computational fluid dynamics has previously been motivated by the need to accurately and efficiently obtain solutions for compressible flow problems. The progress made over the past decade has made it possible to accurately predict compressible three-dimensional viscous flows over complex configurations [1]. As a consequence, methods for solving the three-dimensional incompressible Navier-Stokes equations have only recently become efficient. For this reason, compressible flow solvers are still often used to simulate low speed flows.

The present work was motivated by an ongoing research program at NASA Langley Research Center to develop a semi-span testing capability for the National Transonic Facility (NTF). This test technique is being investigated as a means to design and optimize high-lift devices at flight Reynolds numbers in a ground test facility. Even though the freestream Mach numbers of interest are around .20, the flow around a transport wing with high lift devices deployed may contain regions of compressible flow [2]. Thus to properly model the flow physics, a compressible flow solver may be required. However, the application of a compressible flow solver at low Mach numbers can be problematic.

At low freestream Mach numbers, it may be expected that the performance of a compressible flow solver will degrade to the point where either the solver becomes inefficient, or accurate solutions may be unobtainable [3,4]. The inefficiency stems from the fact that the allowable local time step is inversely proportional to the local speed of sound [5]. Decreasing the freestream Mach number effectively reduces the maximum allowable time step, which translates directly into increased solution times. It can also be shown that in the limit as

the freestream Mach number goes to zero, the solution of the governing equations become singular [6]. For these reasons, it is necessary to determine at what freestream Mach number a particular compressible flow solver becomes inefficient or inaccurate.

Recently, several researchers have investigated the performance of compressible flow solvers at low freestream Mach numbers [3,4]. While quite informative, the geometries used for the computations were two-dimensional. The objective of this phase of the project is to directly compare the performance of two widely used three-dimensional compressible Navier-Stokes solvers at low Mach numbers to both experimental data and to results obtained from an incompressible Navier-Stokes solver. The geometries of interest are two isolated wings with different leading edge sweep angles [7]. The compressible Navier-Stokes solvers chosen, TLNS3D-MB [8] and CFL3D [9], which were developed at NASA Langley Research Center (LaRC), represent the current state-of-the-art in compressible 3-D Navier-Stokes solvers. The incompressible Navier-Stokes solver, INS3D-UP [10], developed recently at NASA Ames Research Center (ARC), represents the current state-of-the-art in incompressible Navier-Stokes solvers.

Geometry discreption and experimental data

The results obtained from all three Navier-Stokes solvers are compared directly to experimental data, for two different geometries. The geometries are isolated wings with taper ratios of unity, and no geometric twist [7]. The first wing geometry is unswept ($\Lambda = 0^\circ$), and is constructed of the NACA 0012 airfoil section. The second wing has a leading edge sweep angle of $\Lambda = 30^\circ$, which is similar to that found on commercial transport aircraft. It should be noted that a wing tip extension was added to the swept wing so that the wing tip would be parallel to the approaching freestream. Both wings have rounded wing tips, and aspect ratios of six. The wings were well instrumented with surface pressure taps at ten spanwise stations. For the unswept cases, the surface pressure data were integrated to give the spanwise variation of normal force.

Computational codes

Both TLNS3D-MB and CFL3D solve the 3-D time dependent thin-layer Navier-Stokes equations, discretized in finite volume form. For steady state solutions, both codes employ several convergence acceleration techniques including multigriding, grid sequencing, and local time stepping. The methods of solution differ however. TLNS3D-MB [8] is a central difference code, with artificial damping in the form of blended second and fourth differences added for stability. The dissipation can either be added in scalar or matrix form. The solution is advanced explicitly to steady state using a five stage Runge-Kutta scheme which is second order accurate. CFL3D [9] is an upwind code, based on Roe's flux difference splitting scheme. The inviscid flux terms are spatially differenced using upwind biasing, while the viscous terms are centrally differenced. The solution is advanced implicitly to steady state by use of a 3-factor approximate factorization which is second order accurate.

INS3D-UP [10] solves the thin-layer incompressible Navier-Stokes equations cast in finite difference form using the method of artificial compressibility. The inviscid flux terms

are upwind biased using Roe’s flux difference splitting scheme, while the viscous terms are centrally differenced. The solution is implicitly advanced to steady state using Gauss-Seidel line relaxation. The resulting solution is second order accurate.

Grid generation

Figure 1 shows partial views of the C-O grids used for both isolated wing geometries. An algebraic grid generation algorithm, based on the transfinite interpolation scheme developed by Eriksson [11], was used to generate the three-dimensional grids. Grid points have been clustered to resolve the large flow gradients in the chordwise, spanwise, and normal directions. For both wing geometries, the upstream and downstream boundaries extend eight root chord lengths from the leading and trailing edges of the wing respectively.

Convergence monitoring

The method of monitoring convergence to steady state differs between the compressible and incompressible flow solvers. Both compressible flow solvers monitor the convergence of the $\partial\rho/\partial t$ term in the continuity equation. The incompressible flow solver, however, monitors the $\partial p/\partial t$ term introduced into the continuity equation by the method of artificial compressibility. Thus, to consistently compare the convergence characteristics of each code, the lift coefficient was monitored.

Results

A grid refinement study has been conducted for both isolated wings using all three codes. For the sake of brevity, only the results obtained for the unswept wing are presented here. It should be noted that the single block version of TLNS3D [12] was used for the present grid refinement study.

Figure 2 compares the computational results from TLNS3D obtained from four grids to experimental data at two spanwise stations on the unswept wing. The flow conditions for this test case are: $M_\infty = .14$, $\alpha = 6.75^\circ$, $Re = 3.3 \times 10^6$. Here η represents the non-dimensional span station. These computations were performed using the Baldwin-Lomax turbulence model, with transition fixed at 5% chord. The grid dimensions, such as $193 \times 49 \times 49$, represent the number of grid points in the streamwise, normal, and spanwise directions respectively. Refinement of the grid clearly improves the agreement with experimental data, particularly at the outboard station. Figure 3 shows comparison of the computed spanwise load distribution to experimental data for the same grids. Here c_n is the local sectional normal force coefficient and C_N the total wing normal force coefficient. Again, grid refinement has improved the agreement with experimental data. With this grid, the typical values of y^+ for the first grid point off the wing surface were in the range of 1-5, with approximately 25 grid points clustered in the wing boundary layer. Figures 4-7 show the same comparisons for CFL3D and INS3D-UP, showing similar grid refinement trends. For these reasons, it was felt that the $193 \times 49 \times 49$ grid was capable of adequately resolving the features of the flowfield.

Figure 8 compares the convergence histories obtained from each code, for the $193 \times 49 \times 49$ grid. As briefly discussed above, the compressible and incompressible flow solvers monitor convergence to steady state in different ways. For consistency, the convergence of the lift coefficient will be used for comparison. The convergence histories are plotted versus the iteration count, but it should be noted that the convergence histories of TLNS3D are typically plotted versus the work unit [12]. The circular symbol on each plot indicates the point at which the lift coefficient has converged to within 1% of the final value. TLNS3D and INS3D-UP show smooth convergence of lift, while CFL3D shows an oscillatory lift convergence. Both compressible flow computations required approximately 2.75 CPU hours on a Cray Y-MP supercomputer to obtain lift convergence. On the other hand, the INS3D-UP computation required approximately 4.75 CPU hours on the same computer. The comparative inefficiency of INS3D-UP may be due to the lack of convergence acceleration techniques such as multigriding. As an example, the addition of multigriding to TLNS3D resulted in an approximate 7-fold reduction in computational time [12].

Figure 9 shows a comparison of the computational results obtained from the three flow solvers to experimental data for the following conditions: $M_\infty = .14$, $\alpha = 6.75^\circ$, $Re = 3.3 \times 10^6$, and $\Lambda = 0^\circ$. Both compressible solutions were obtained using the Baldwin-Lomax (B-L) turbulence model, while INS3D-UP used the Baldwin-Barth (B-B) turbulence model. For an attached flow field, it is expected that the performance of both turbulence models will be similar [13]. At the inboard station, the computational results are nearly identical, and agree quite well with the experimental data. At the outboard station the computations show some differences, however, the predicted pressure distributions are still in good agreement with the data. All three codes have underpredicted the influence of the tip vortex, as seen in the experimental data near the trailing edge. From this comparison it is seen that all three computations consistently predict higher pressures. The mismatch of pressures on the lower surface may indicate that the angle of attack for the computations was lower than the effective experimental angle of attack. It should be noted that the experimental data has not been corrected for wind tunnel blockage effects [7].

Figure 10 compares the computed spanwise load distributions to experimental data for the same case. The agreement over the entire wing surface is quite good. The TLNS3D prediction shows the best agreement, particularly over the outer 25% of the wing. All three computations underpredict the load distribution on the outboard portion of the wing. This again is attributable to the uncorrected experimental angle of attack. Both compressible flow solvers predict a sharp peak near the tip, while the incompressible solver predicts only a small discontinuity. Further experimental data would be required to determine which flow solver best models the physics of the tip vortex.

Figure 11 compares the computed pressure distributions to experimental data at two spanwise locations for the swept wing geometry. The conditions for this case are: $M_\infty = .14$, $\alpha = 6.75^\circ$, $Re = 3.3 \times 10^6$, and $\Lambda = 30^\circ$. Here η' is the non-dimensional span location, measured *along* the leading edge. The pressure taps are no longer parallel to the approaching flow, but are perpendicular to the wing leading edge. At the inboard station, all three computations are nearly identical, and show good agreement with the data. At the outboard station, the computations show some differences, most notably in the prediction of the leading edge suction peak. Both upwind predictions (CFL3D, INS3D-UP) show slightly better performance than the central difference solution of TLNS3D. This may be due to the

artificial dissipation added to the TLNS3D solution. It should be noted that this version of TLNS3D employs only the scalar form of dissipation, and it is expected that the matrix form of dissipation would give improved performance [14]. As with the unswept case, the mismatch of pressures, particularly on the lower surface, again may indicate the effective experimental angle of attack was slightly higher.

These two test cases have shown that both compressible flow solvers are capable of accurately predicting the low speed flow around the 3-D wing geometries for the given freestream Mach number. The convergence histories and flow field solutions showed no oscillations, indicating that no numerical difficulties are encountered for the low freestream Mach number of interest. The solutions obtained using the compressible flow solvers have been found to be nearly identical to those obtained using the incompressible flow solver.

To examine the influence of Mach number on the performance of the compressible flow solvers, TLNS3D was run at systematically lower Mach numbers. Even though experimental data was not available for comparison, the accuracy and efficiency of the code can still be examined. The freestream Mach numbers chosen were: .100, .075, .050, .025, and .010. Figure 12 compares the computed results to the $M_\infty = .14$ results discussed above. Initially as the Mach number decreases, from .140 to .075, the predicted pressures become more positive following the expected trend. Over this range, there are no signs of oscillations present in the solution. As the Mach number is decreased to .050, small amplitude oscillations begin to appear at the outboard station. As the freestream Mach number is further decreased to .025, low amplitude oscillations are also observed at the inboard station. The oscillations appear to damp out at around 50% chord at both stations. As the Mach number decreases further, the solution degrades to the point where oscillations cover the entire surface.

Figure 13 examines the influence of Mach number on the convergence histories in terms of the residual of the continuity equation. As expected, the convergence rate deteriorates as the Mach number is decreased. However, the smooth convergence histories do not reflect the oscillatory behavior seen in the pressure distributions at the lower Mach numbers. The convergence histories of the lift coefficient give a more accurate assessment of convergence. Figure 14 shows the lift convergence histories for each case. From this figure, only the two highest Mach number cases are considered well converged. As Mach number decreases, the rate of convergence clearly deteriorates.

This preliminary analysis has shown that the compressible flow solver TLNS3D yields accurate solutions at Mach number as low as .075 with no apparent computational difficulties. The code is also found to be computationally efficient, and thus suited for conducting parametric studies. However, the influence of matrix dissipation on the low Mach number performance of TLNS3D needs to be examined.

Future work

Free-air computations

At present, a grid refinement study is being conducted for the EET semi-span geometry using TLNS3D-MB. The fuselage centerline plane is treated with symmetry boundary conditions, which effectively models the full-span configuration. These “ree-air” computations

will serve two purposes. First, the computations will provide a baseline which will be used to determine what influence the sidewall boundary layer has on the flow over the model. The free-air computations will be validated by making direct comparison with the available full-span experimental data [15]. The second purpose of the free-air computations is to provide detailed information which will not be easily obtainable in the wind tunnel testing in the NTF. This data will also provide an independent method for evaluating the quality of the experimental data.

Viscous sidewall modeling

The viscous sidewall computations are the primary focus of the research project. The goal is to examine in detail, what influence the sidewall boundary layer has on the flow over the semi-span model. This determination will be made by making direct comparison with the free-air computations, and available experimental data. The comparisons will be made on several levels. The most general comparisons will be between force and moment coefficients, and will give an overall assessment of the influence of the sidewall boundary layer. Detailed comparisons between surface pressure distributions, over the entire model, will give insight as to how the flow field has been modified by the presence of the sidewall boundary layer. The finest level of comparison would examine details of the wing and fuselage boundary layers, and how they have been influenced by the sidewall boundary layer.

The predicted behavior of the sidewall boundary layer is of particular interest. Due to the difficulty in obtaining off-surface measurements in the cryogenic environment, little experimental data can be obtained to characterize the behavior of the sidewall boundary layer. In this particular aspect, the computations will give insight into the inherent juncture flow present in semi-span testing. If the predicted characteristics of the sidewall boundary layer are not acceptable, such as the formation of horseshoe vortices, techniques to improve the flow quality can be computationally examined (such as suction, tangential blowing, or vortex generators).

Acknowledgements

This work was supported by Cooperative Agreement NCC1-169 between North Carolina State University and the High Reynolds Number Aerodynamics Branch at NASA Langley Research Center. The authors thank Jassim A. Al-Saadi for many insightful comments regarding the computational results. The authors are grateful to Veer N. Vatsa, Sherri Krist, and Stuart Rogers for many helpful discussions regarding the three Navier-Stokes solvers. The authors would also like to thank L. Elwood Putnam for his support of this work.

References

1. Dominik, D., Rajagopal, K., Vuong, S., Wisneski, J., Olling, C., Hock, G., and Sikora, J., "Navier-Stokes Solution for the Space Shuttle Vehicle Using a Full-Scale High Fidelity Grid Model," AIAA Paper 93-0419, January 1993.

2. Squire, L.C., "*Interactions Between Wakes and Boundary-Layers*," Progress in Aerospace Science, Vol. 26, pp. 261-288, 1989.
3. Volpe, G., "*Performance of Compressible Flow Codes at Low Mach Numbers*," AIAA Journal, Vol. 31, January 1993, pp. 49-56.
4. Choi, Y.H. and Merkle, C.L., "*The Application of Preconditioning in Viscous Flows*," Journal of Computational Physics, Vol. 105, April 1993, pp. 207-223.
5. Anderson, D.A, Tannehill, J.C. and Pletcher, R.H., "*Computational Fluid Mechanics and Heat Transfer*," Hemisphere Publishing Corporation, New York, 1984.
6. Pletcher, R.H. and Chen, K.H., "*On Solving The Compressible Navier-Stokes Equations for Unsteady Flows at Very Low Mach Numbers*," AIAA Paper 93-3368-CP, July 1993.
7. Yip, L.P and Shubert, G.L., "*Pressure Distributions on a 1-by-3 Meter Semispan Wing at Sweep Angles From 0° to 40° in Subsonic Flow*," NASA TN D-8307, December 1976.
8. Vatsa, V.N., Sanetrik, M.D., and Parlette, E.B., "*Development of a Flexible and Efficient Multigrid-Based Multiblock Flow Solver*," AIAA Paper 93-0677, January 1993.
9. Thomas, J.L., Taylor, S.L. and Anderson, W.K., "*Navier-Stokes Computations of Vortical Flows Over Low Aspect Ratio Wings*," AIAA Paper 87-0207, January 1987.
10. Rogers, S.E., "*Progress in High-Lift Aerodynamic Calculations*," AIAA Paper 93-0194, January 1993.
11. Eriksson, L.E., "*Generation of Boundary-Conforming Grids Around Wing-Body Configurations Using Transfinite Interpolation*," AIAA Journal, Vol. 20, October 1982, pp. 1313-1320.
12. Vatsa, V.N. and Wedan, B.W., "*Development of an Efficient Multigrid Code for 3-D Navier-Stokes Equations*," AIAA Paper 89-1791, June 1989.
13. Yu, N.J., Allmaras, S.R., and Moschetti, K.G., "*Navier-Stokes Calculations for Attached and Separated Flows Using Different Turbulence Models*" AIAA Paper 91-1791, June 1991.
14. Turkel, E. and Vatsa, V.N. , "*Effect of Artificial Viscosity on Three Dimensional Flow Solutions*," AIAA Paper 90-1444, June 1990.
15. Morgan Jr.,H.L., "*Model Geometry Description and Pressure Distribution Data From Tests of EET High-Lift Research Model Equipped with Full-Span and Part-Span Flaps*," NASA TM 80048, February 1979.

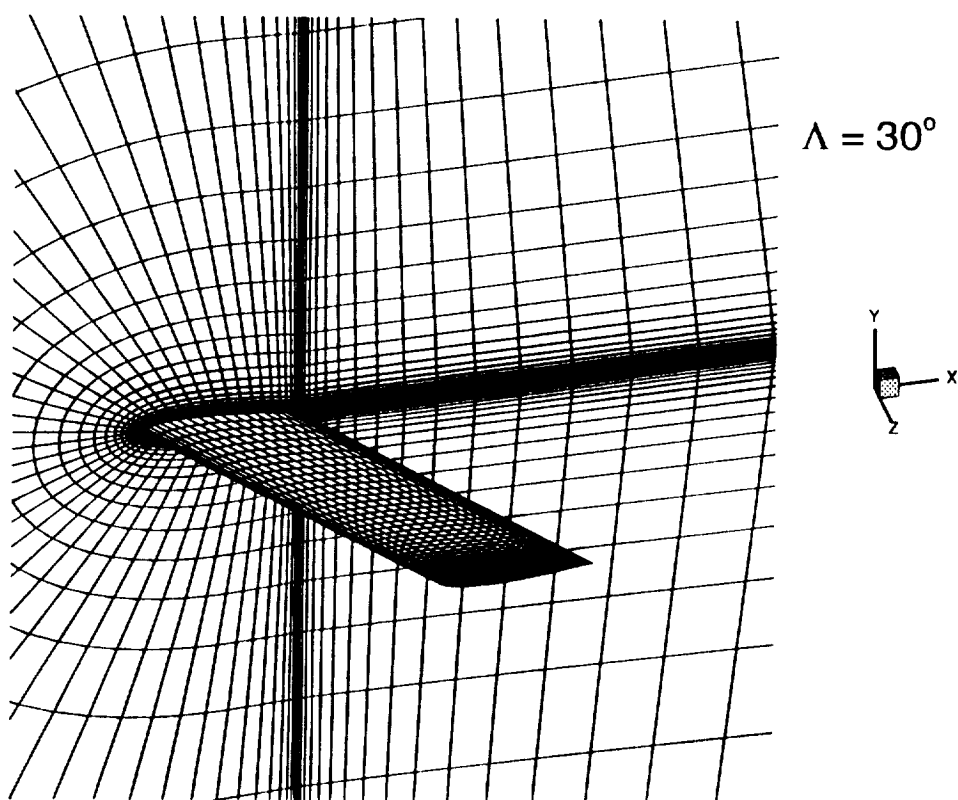
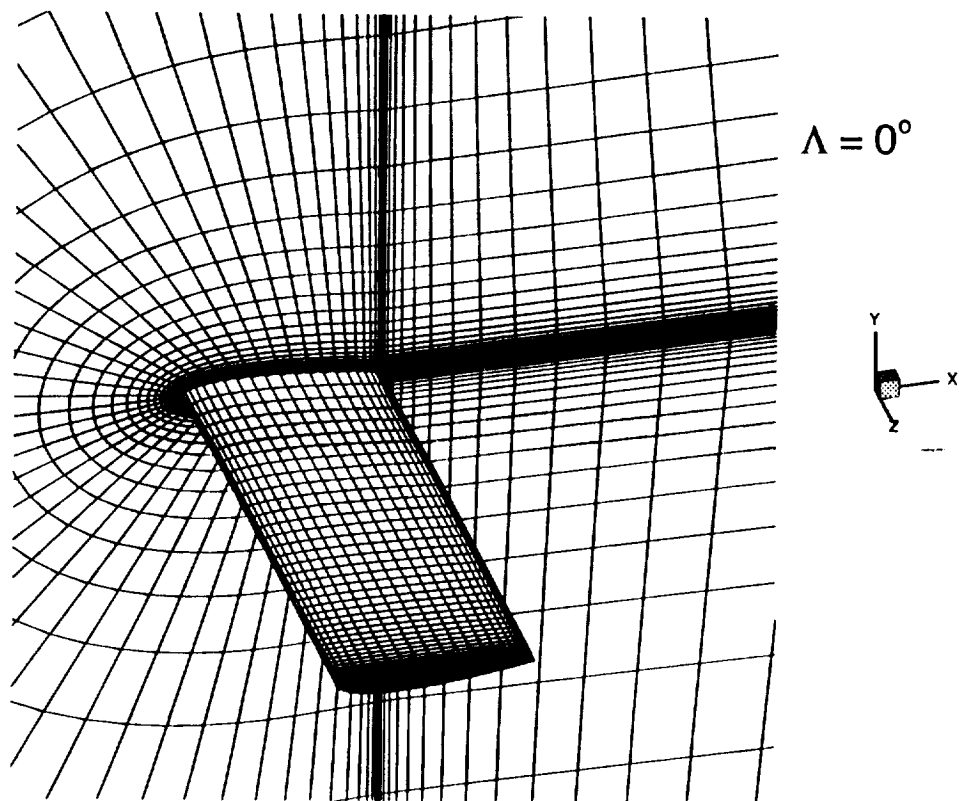


Fig. 1: Partial view of C-O grid topologies for isolated wing geometries.

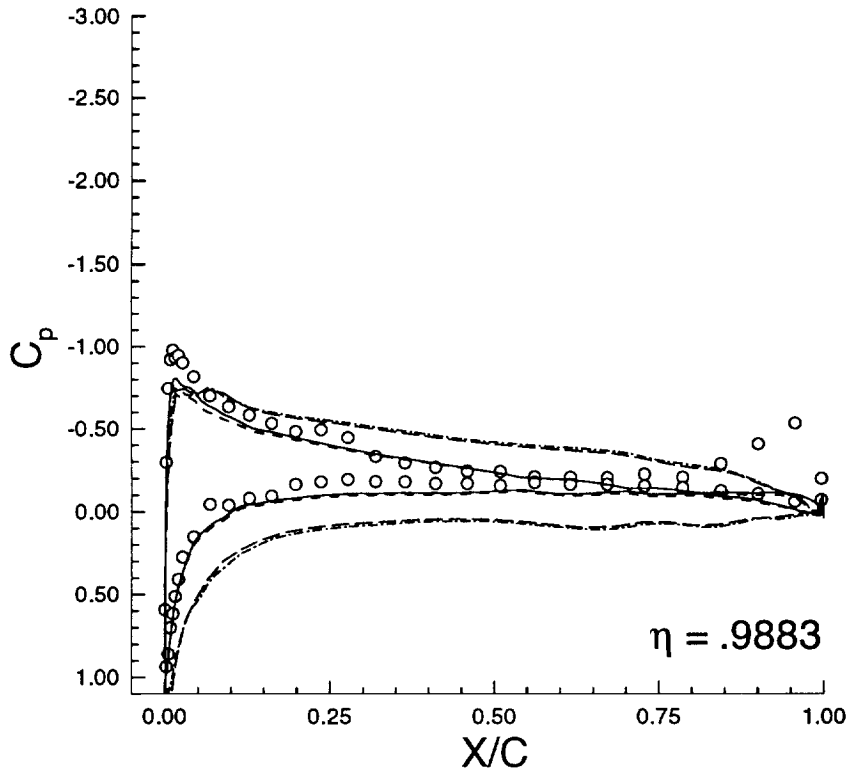
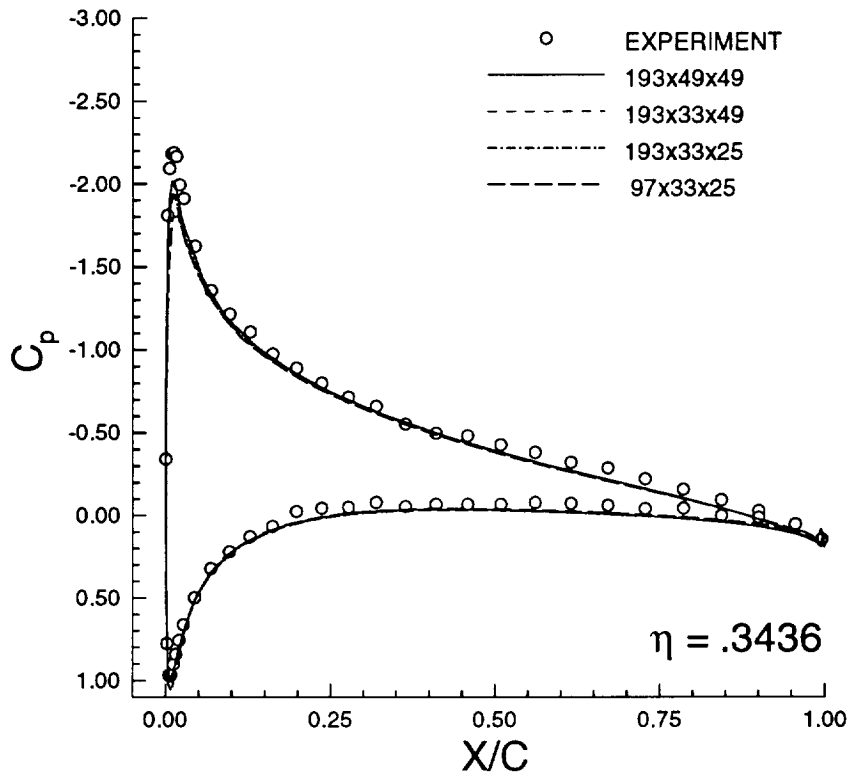


Fig. 2: Influence of grid refinement on computed pressure distributions, TLNS3D ($M_\infty = .14$, $\alpha = 6.75^\circ$, $Re = 3.3 \times 10^6$, $\Lambda = 0^\circ$).

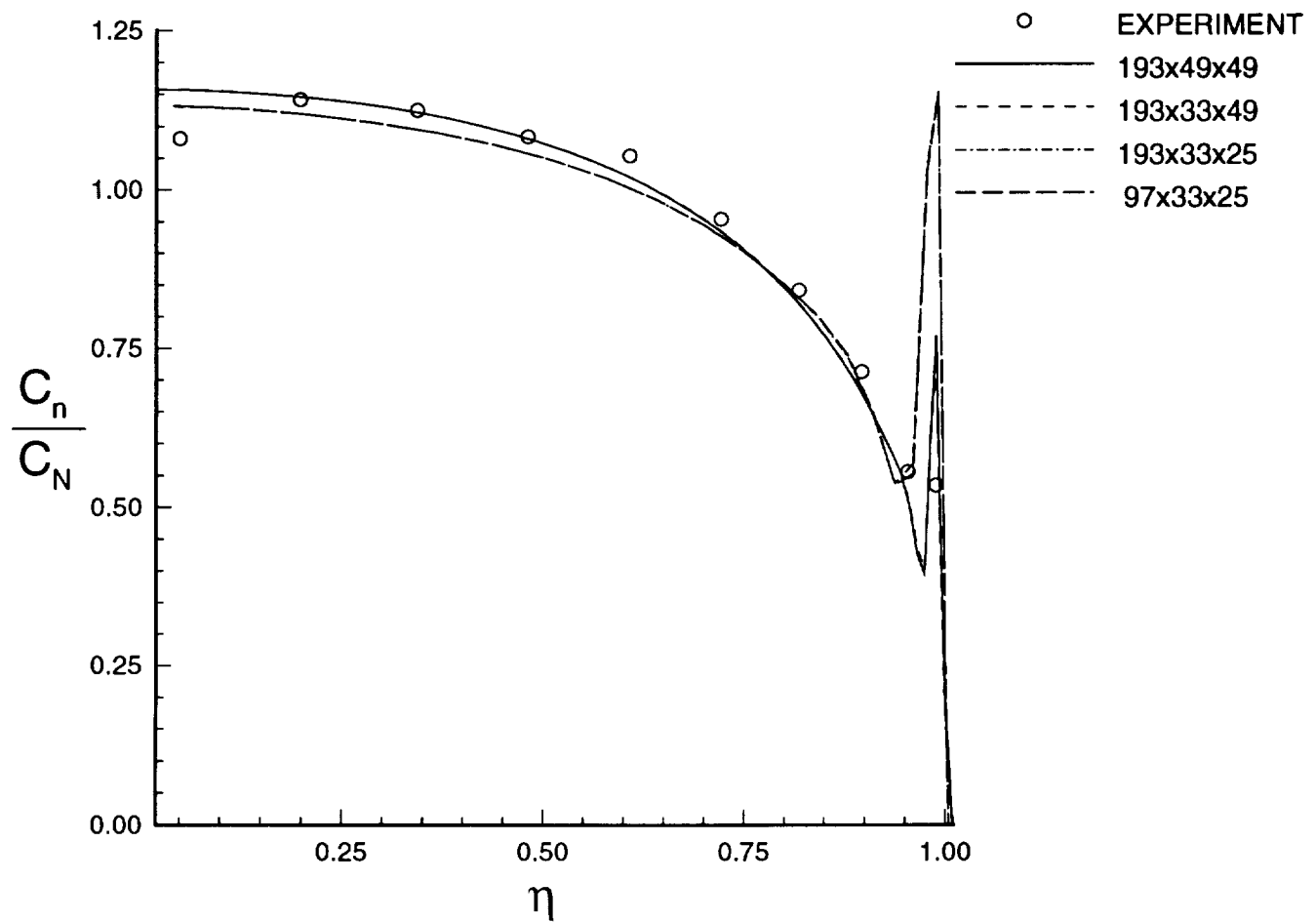


Fig. 3: Influence of grid refinement on computed spanwise load distributions, TLNS3D ($M_\infty = .14$, $\alpha = 6.75^\circ$, $Re = 3.3 \times 10^6$, $\Lambda = 0^\circ$) .

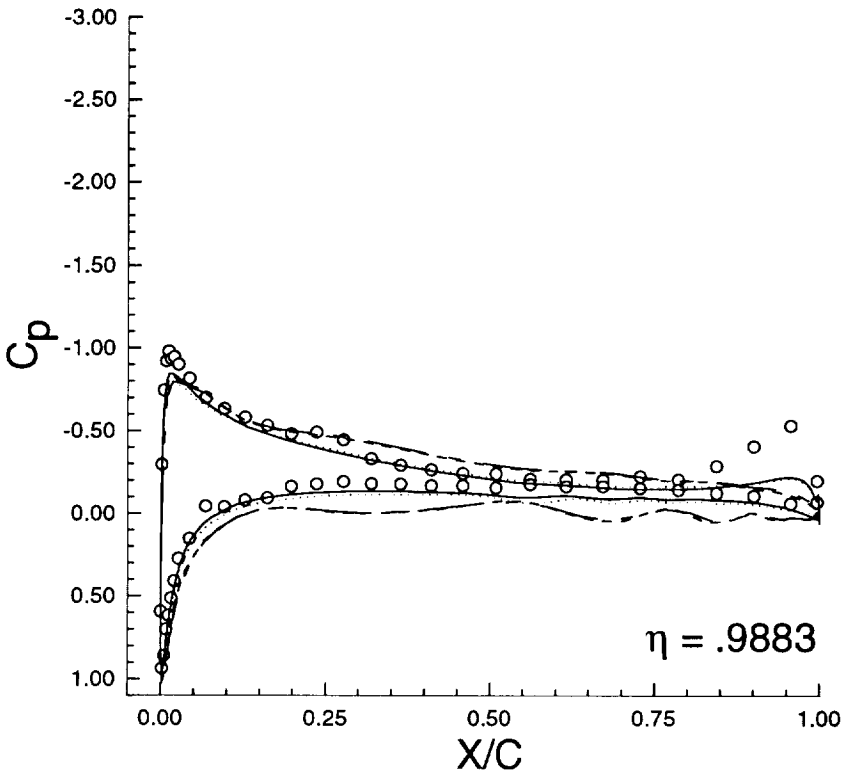
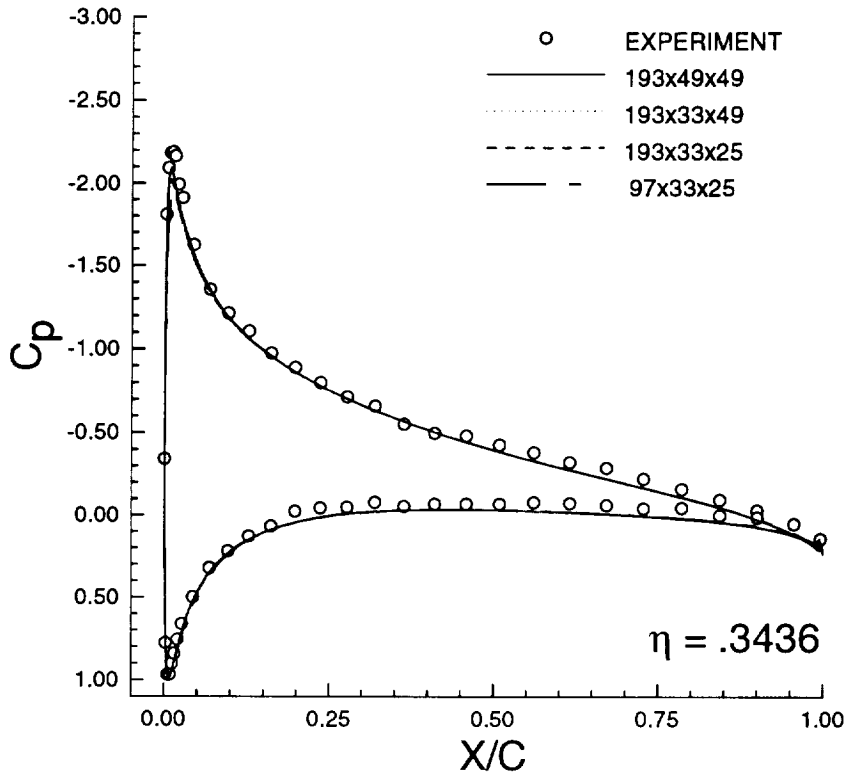


Fig. 4: Influence of grid refinement on computed pressure distributions, CFL3D ($M_\infty = .14$, $\alpha = 6.75^\circ$, $Re = 3.3 \times 10^6$, $\Lambda = 0^\circ$).

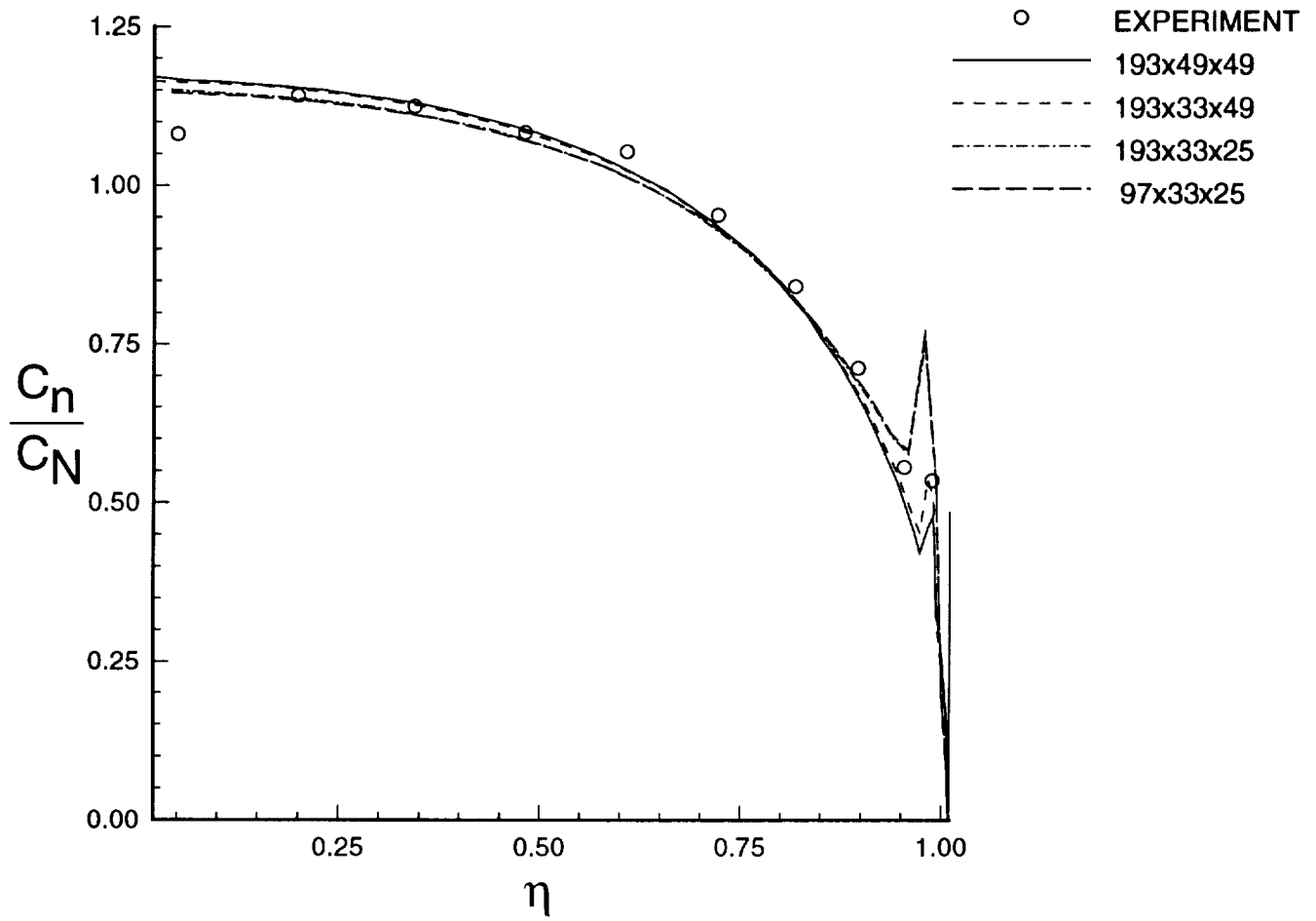


Fig. 5: Influence of grid refinement on computed spanwise load distributions, CFL3D ($M_\infty = .14$, $\alpha = 6.75^\circ$, $Re = 3.3 \times 10^6$, $\Lambda = 0^\circ$) .

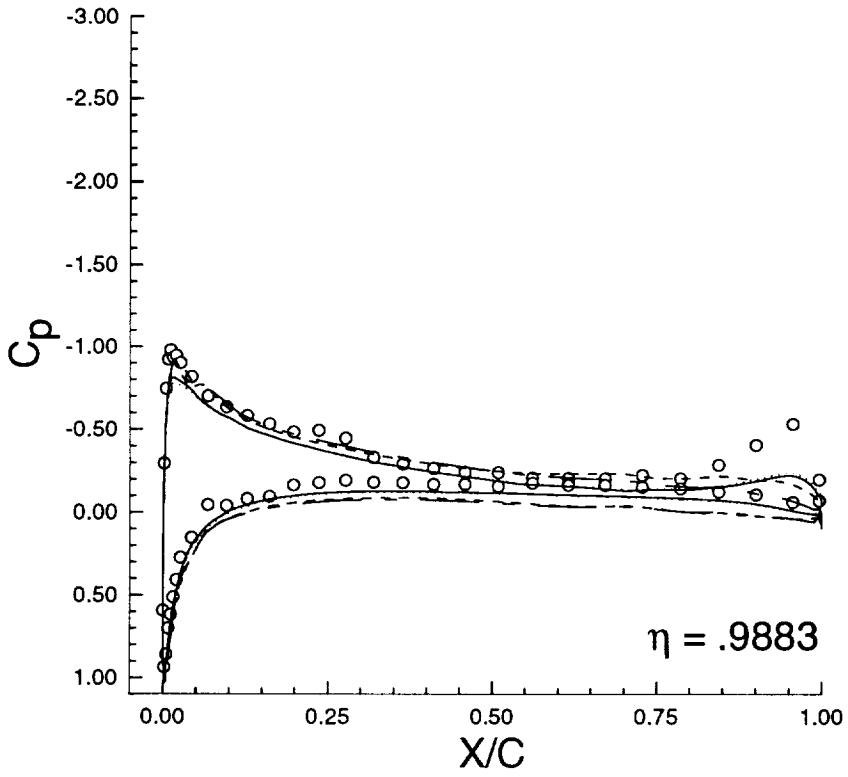
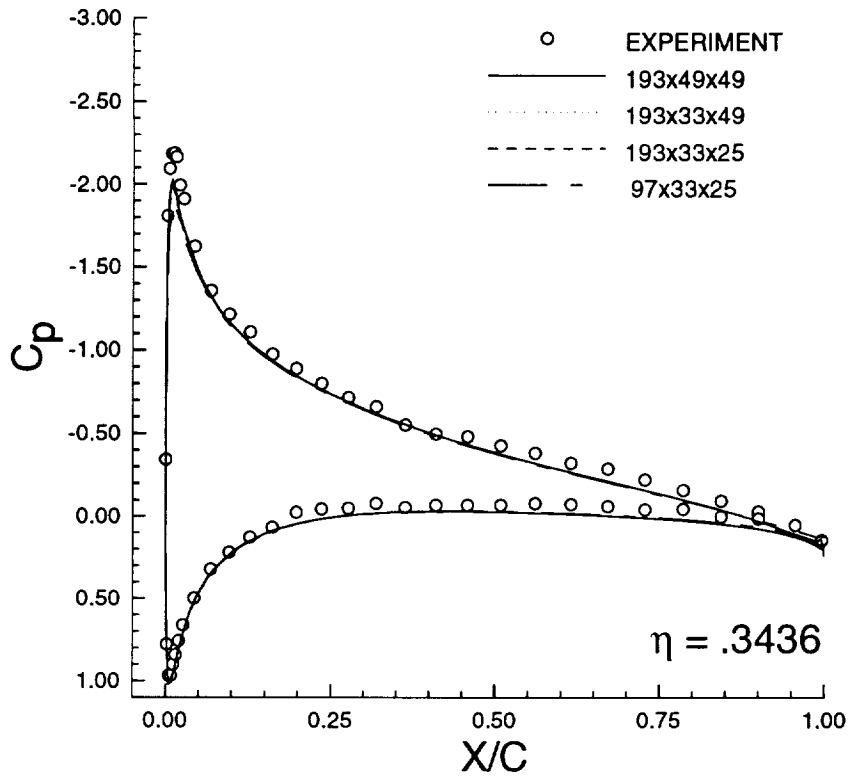


Fig. 6: Influence of grid refinement on computed pressure distributions, INS3D-UP ($M_\infty = .14$, $\alpha = 6.75^\circ$, $Re = 3.3 \times 10^6$, $\Lambda = 0^\circ$).

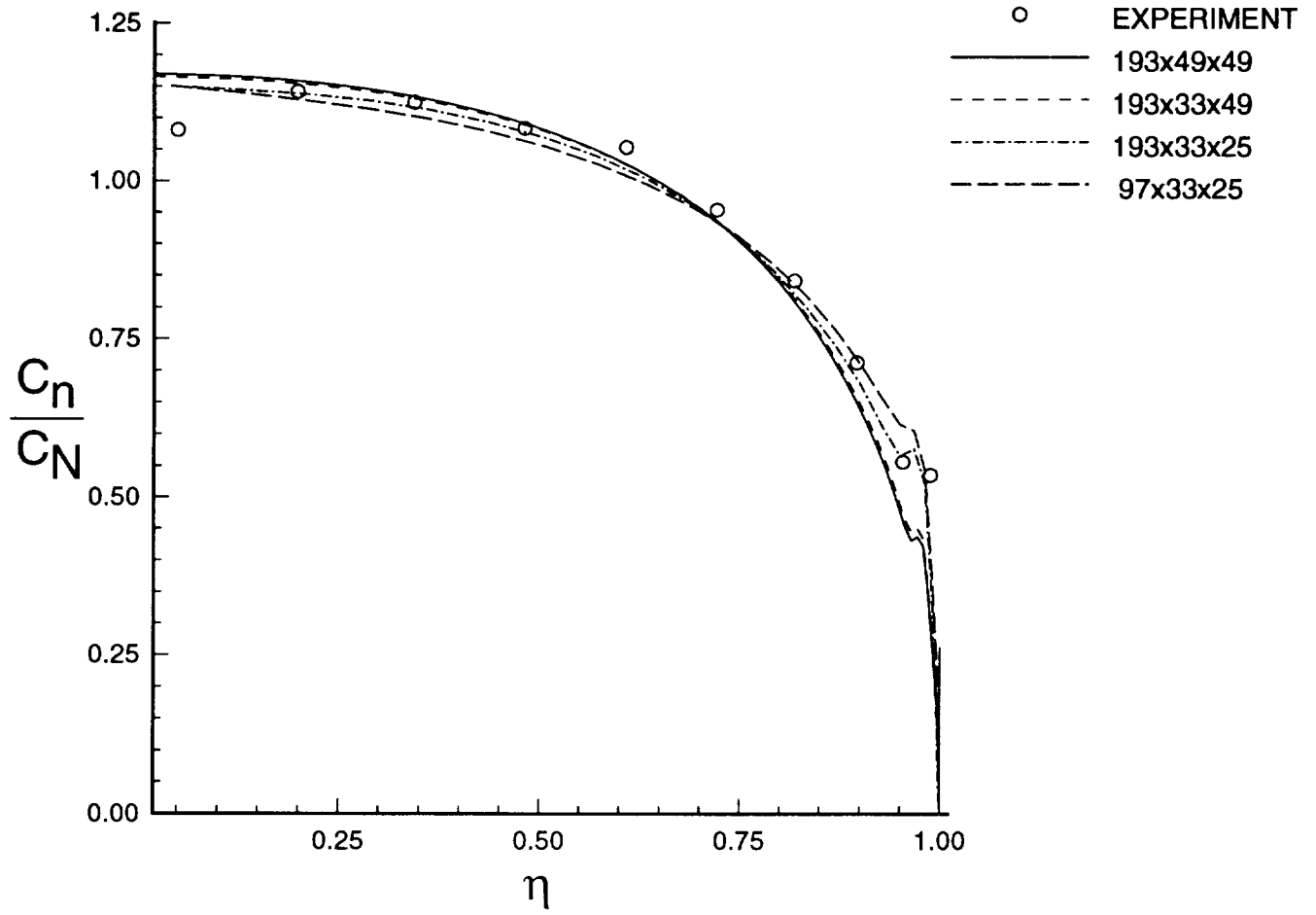


Fig. 7: Influence of grid refinement on computed spanwise load distributions, INS3D-UP ($M_\infty = .14$, $\alpha = 6.75^\circ$, $Re = 3.3 \times 10^6$, $\Lambda = 0^\circ$).

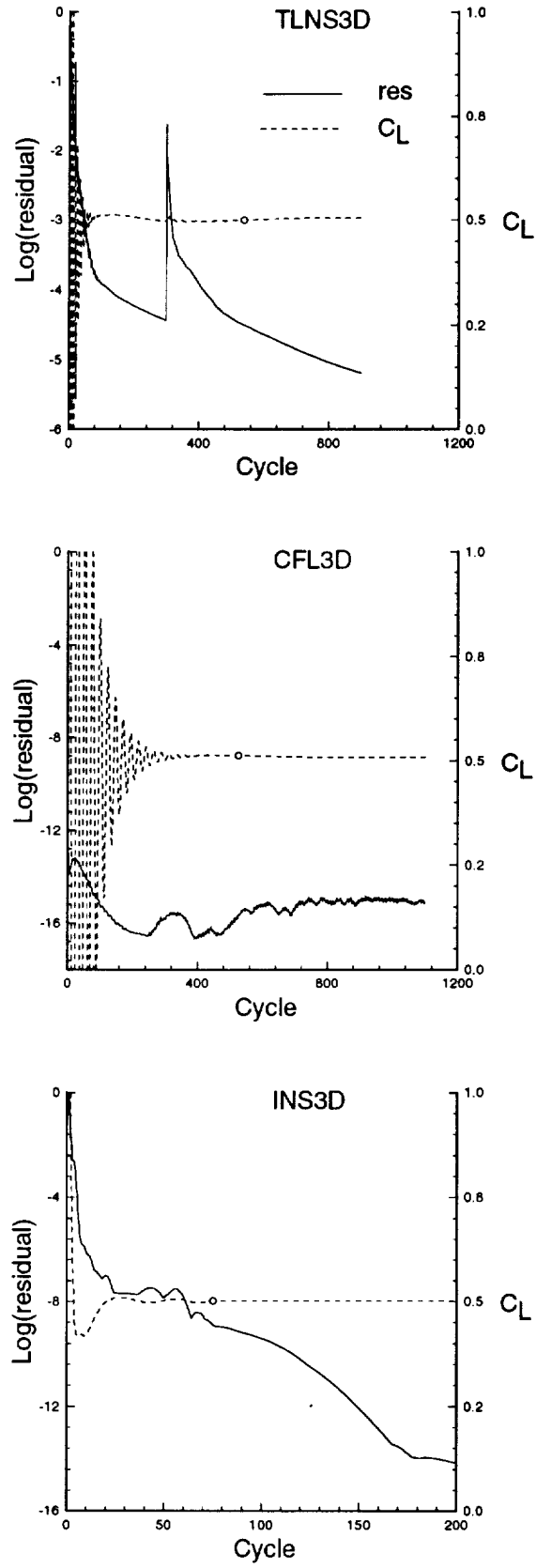


Fig. 8: Convergence histories for $193 \times 49 \times 49$ grid
 $(M_\infty = .14, \alpha = 6.75^\circ, \text{Re} = 3.3 \times 10^6, \Lambda = 0^\circ)$.

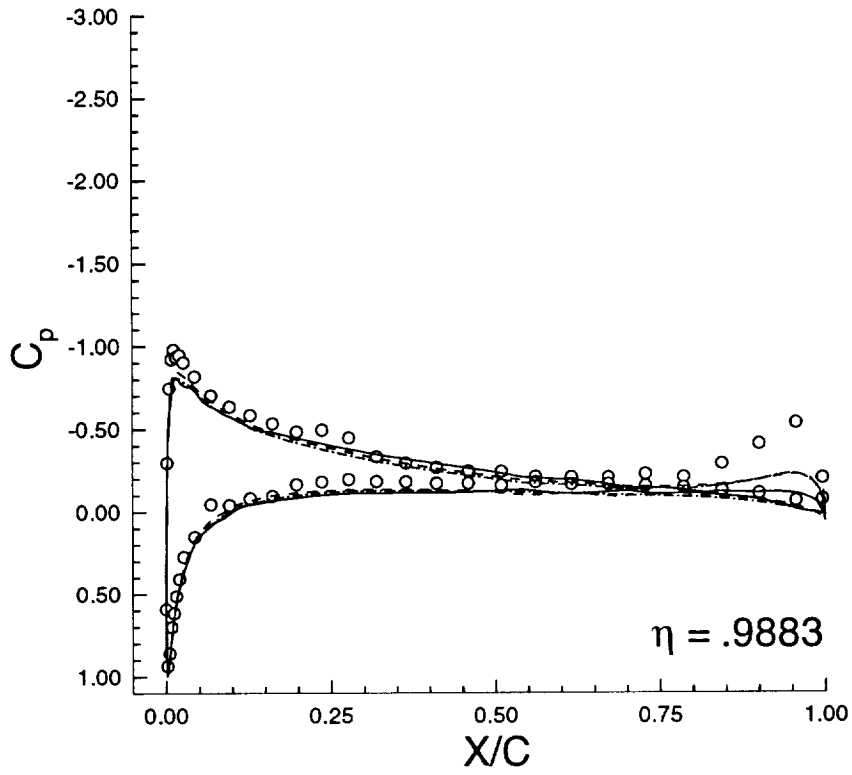
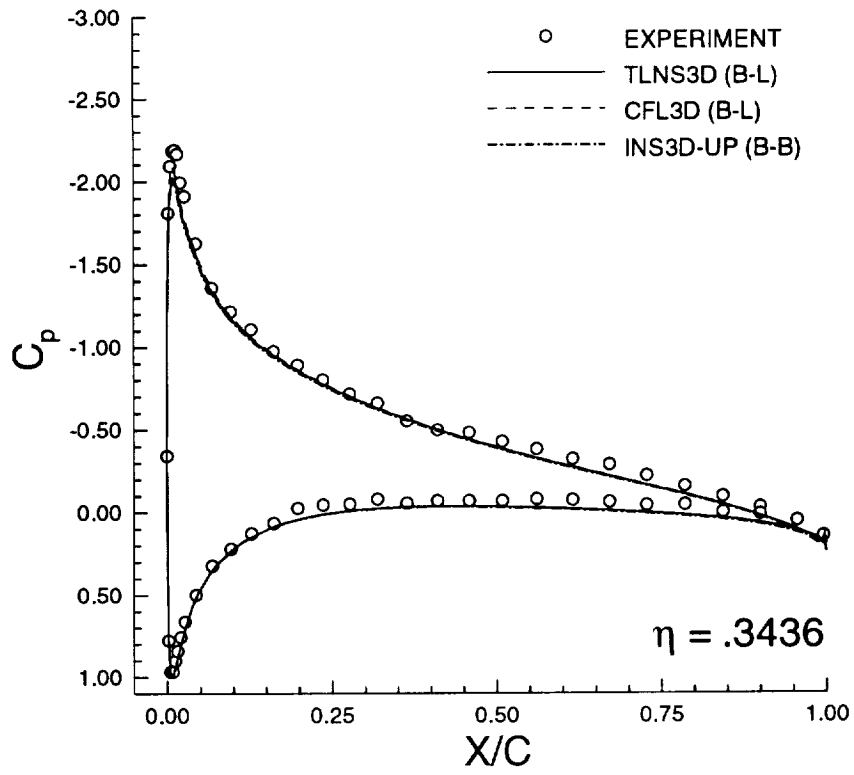


Fig. 9: Comparison of computed pressure distributions with experimental data ($M_\infty = .14$, $\alpha = 6.75^\circ$, $Re = 3.3 \times 10^6$, $\Lambda = 0^\circ$).

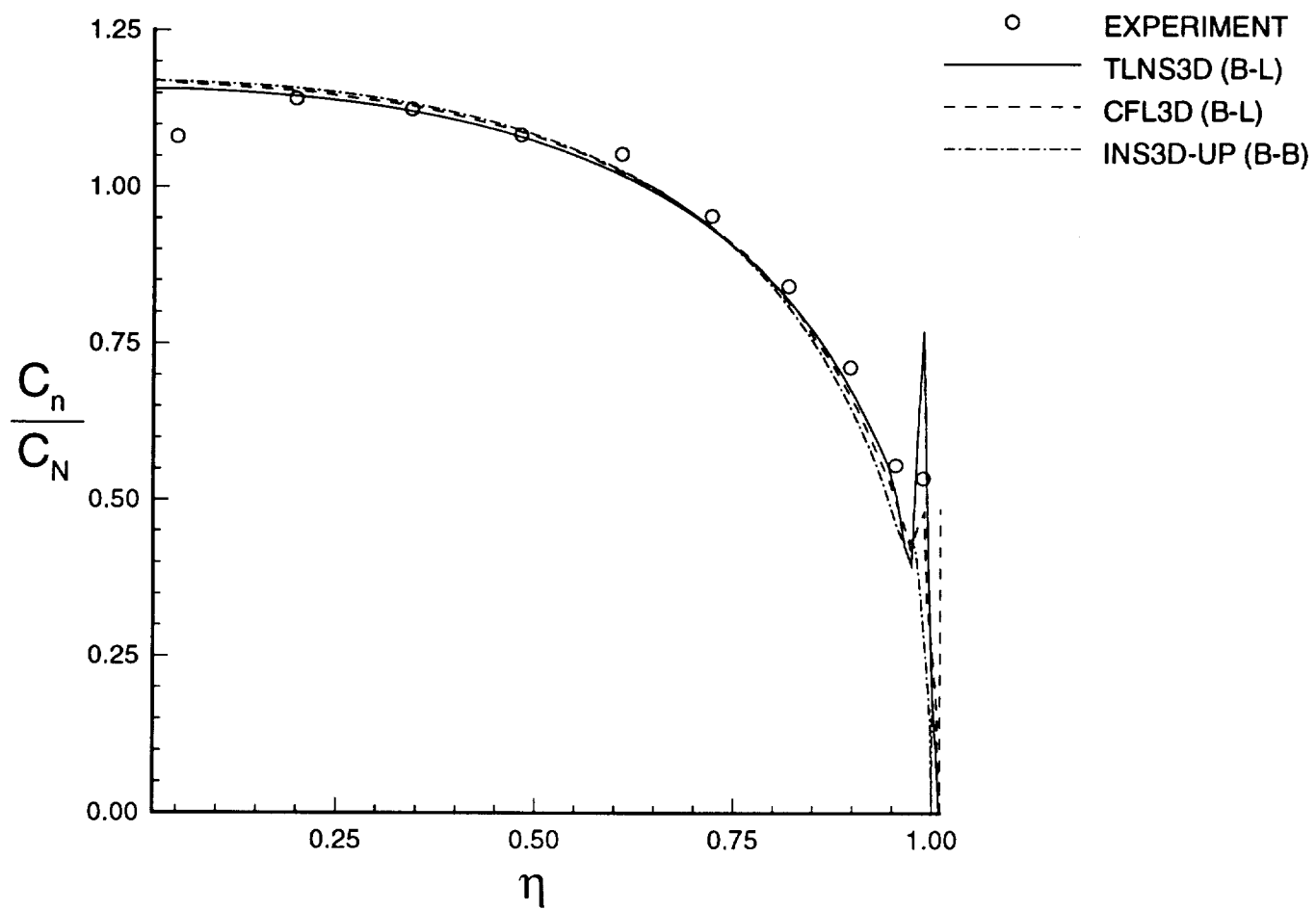


Fig. 10: Comparison of computed spanwise load distributions with experimental data ($M_\infty = .14$, $\alpha = 6.75^\circ$, $Re = 3.3 \times 10^6$, $\Lambda = 0^\circ$) .

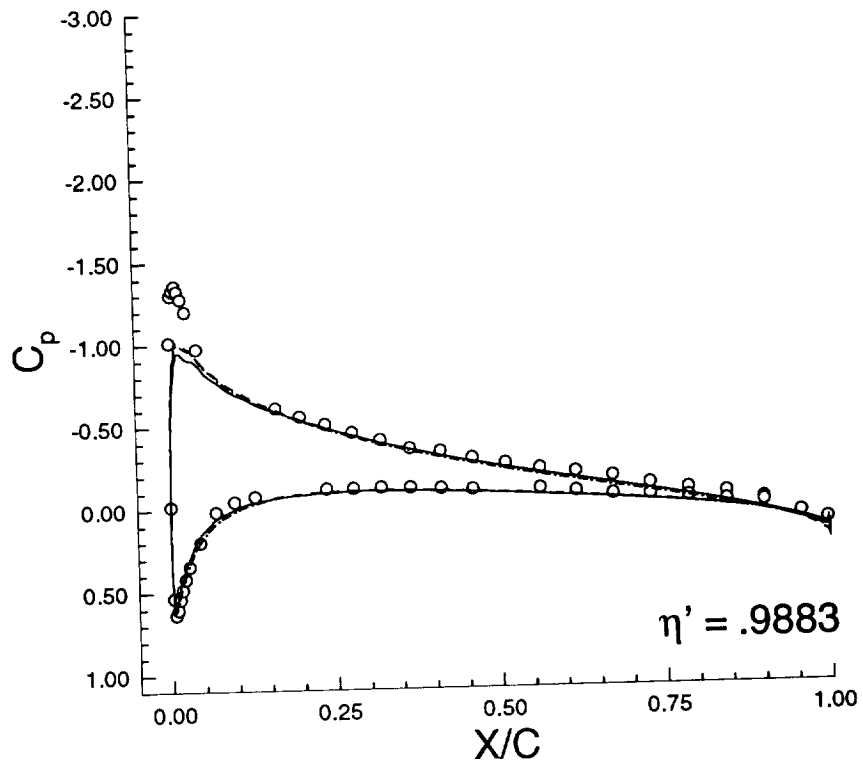
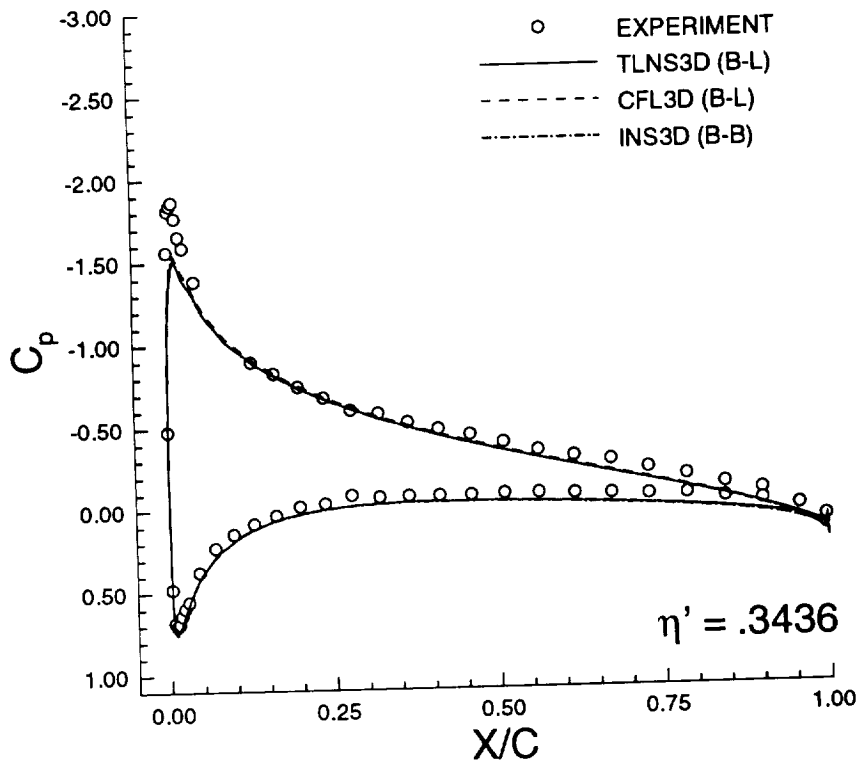


Fig. 11: Comparison of computed pressure distributions with experimental data ($M_\infty = .14$, $\alpha = 6.75^\circ$, $Re = 3.3 \times 10^6$, $\Lambda = 30^\circ$).

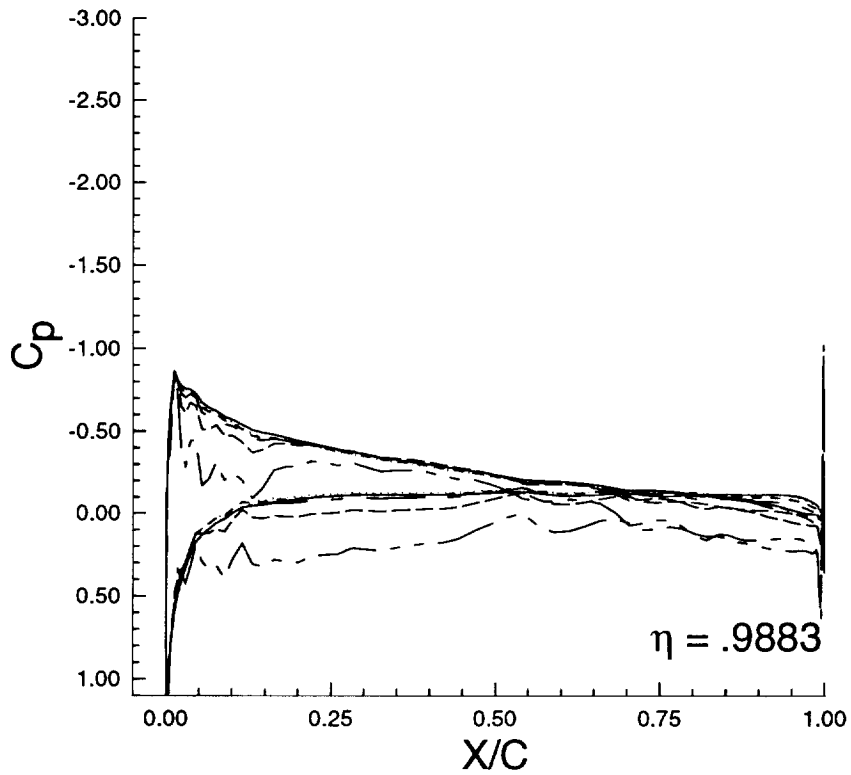
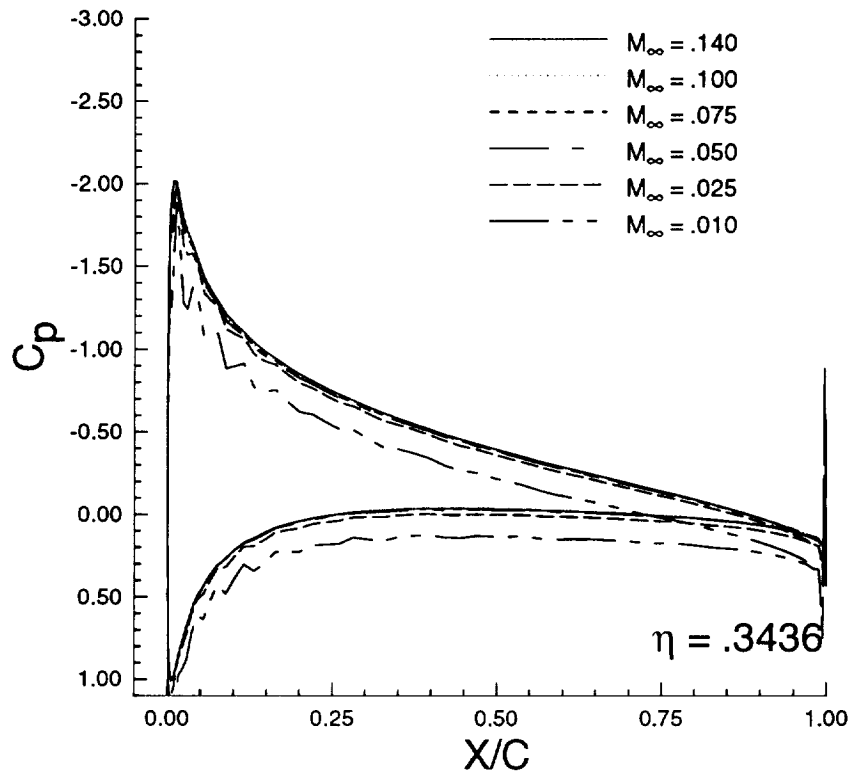


Fig. 12: Influence of Mach number on computed pressure distributions ($M_\infty = .14$, $\alpha = 6.75^\circ$, $Re = 3.3 \times 10^6$, $\Lambda = 0^\circ$).

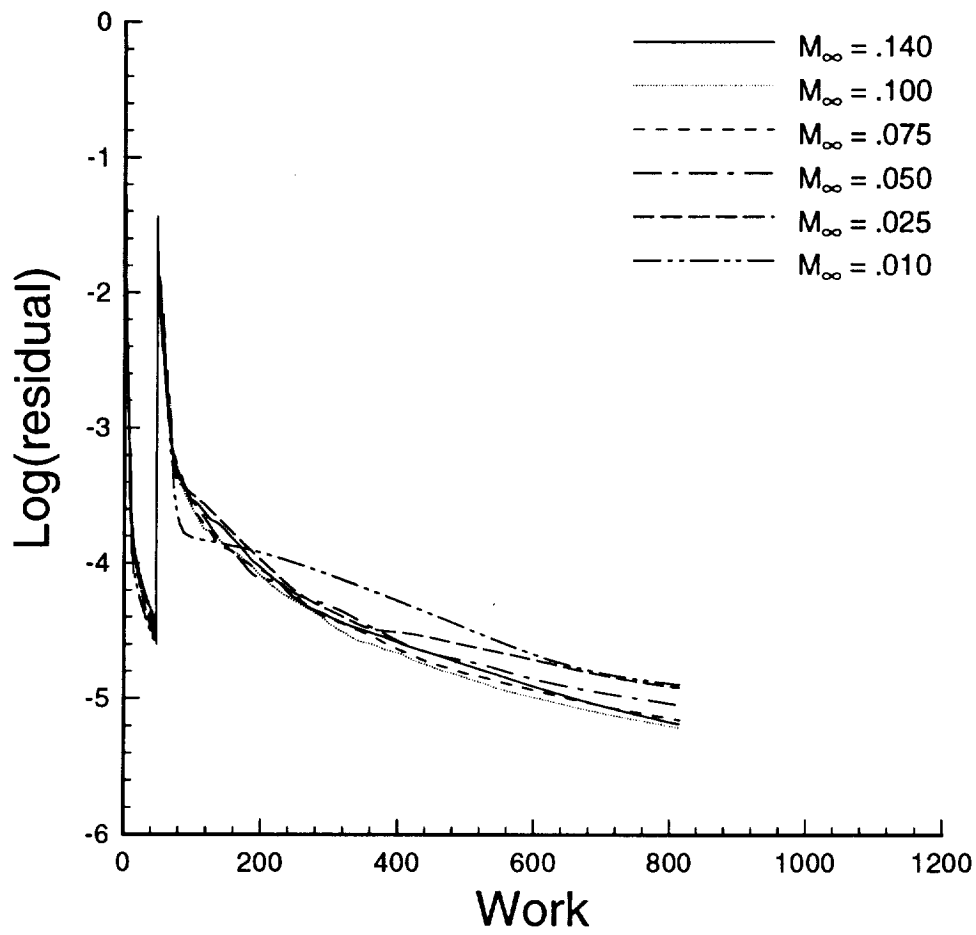


Fig. 13: Influence of Mach number on residual convergence
($M_\infty = .14$, $\alpha = 6.75^\circ$, $Re = 3.3 \times 10^6$, $\Lambda = 0^\circ$) .

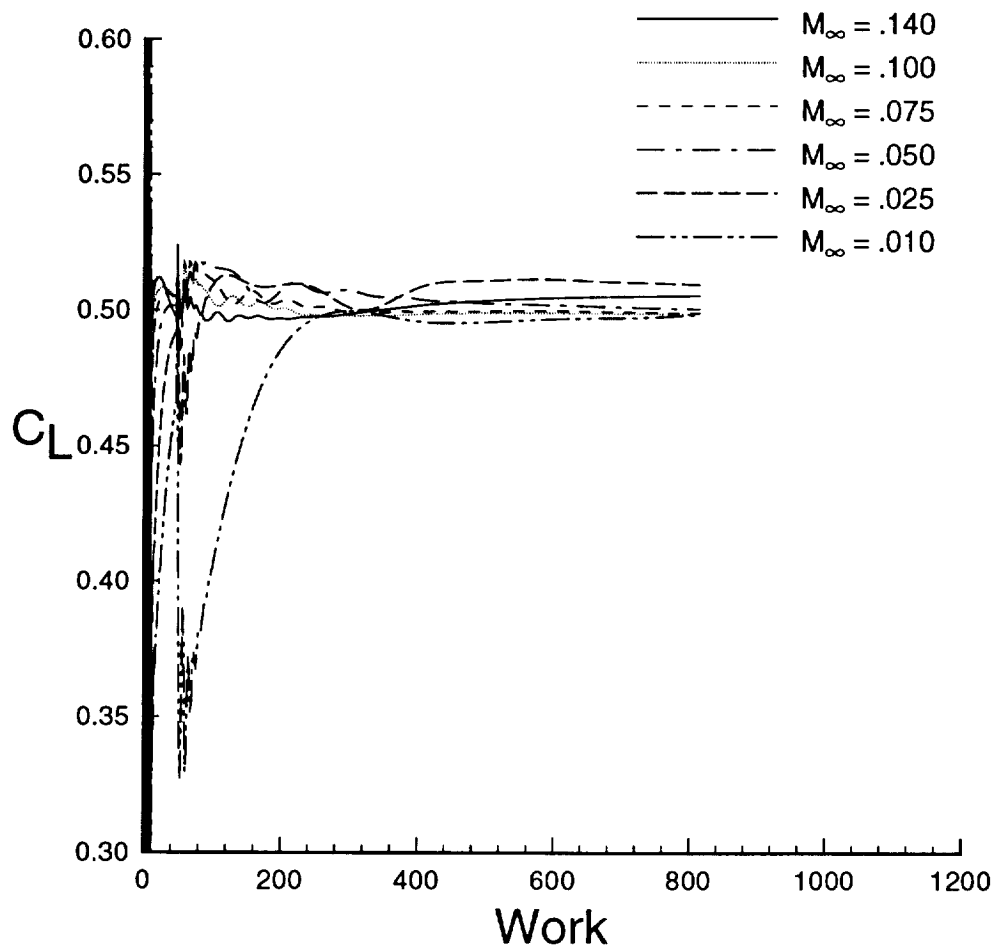


Fig. 14: Influence of Mach number on lift convergence
 $(M_\infty = .14, \alpha = 6.75^\circ, Re = 3.3 \times 10^6, \Lambda = 0^\circ)$.